Journal of Alloys and Compounds 921 (2022) 166040

Contents lists available at ScienceDirect

Journal of Alloys and Compounds

journal homepage: www.elsevier.com/locate/jalcom

Exploring V-Fe-Co-Ni-Al and V-Fe-Co-Ni-Cu high entropy alloys for magnetocaloric applications

Bruno G.F. Eggert[a], Erna K. Delczeg-Czirjak[b], Fernando Maccari[c], Susmit Kumar[d], Oliver Gutfleisch[c], Helmer Fjellvåg[d], Bjørn C. Hauback[a], Christoph Frommen[a,*]

[a] Department for Hydrogen Technology, Institute for Energy Technology (IFE), P.O. Box 40, NO-2027 Kjeller, Norway
[b] Department of Physics and Astronomy, Uppsala University, Box 516, 751 20 Uppsala, Sweden
[c] Functional Materials,Materials Science, Technical University of Darmstadt, 64287 Darmstadt, Germany
[d] Department of Chemistry, University of Oslo, Sem Sælands vei 26, 0371 Oslo, Norway

ARTICLE INFO

Article history:
Received 23 February 2022
Received in revised form 21 June 2022
Accepted 23 June 2022
Available online 29 June 2022

Keywords:
Magnetocaloric
Transition metal alloys and compounds
X-ray diffraction
Scanning electron microscopy
Computer simulations
Magnetism

ABSTRACT

A series of V_{1-x}-Fe-Co-Ni-Al_{1+x} and V_{1-x}-Fe-Co-Ni-Cu_{1+x} high entropy alloys with varying compositions ($0 \leq x \leq 0.75$) has been investigated for magnetocaloric applications. Compositions were selected according to established properties, such as configurational entropy, atomic size difference, and enthalpy of mixing. To study the influence of composition on magnetic ordering temperatures, the V and (Al/Cu) contents were changed while the content of Fe, Co and Ni was retained at 20 at. % each. The crystal structure and microstructure of the as-cast alloys were compared to literature phase guidelines and thermodynamic calculations based on the CALPHAD approach. The V-Fe-Co-Ni-Al compounds are monophasic and crystallize in a disordered body centered cubic structure or its ordered B2 variant, while the V-Fe-Co-Ni-Cu compounds are all multiphasic. Magnetic transitions in the V-Fe-Co-Ni-Al system span over 400 K, with Curie temperature ranging from 155 K in equiatomic VFeCoNiAl, to 456 K in non-equiatomic $V_{0.25}$FeCoNi$Al_{1.75}$. The V-Fe-Co-Ni-Cu alloys display magnetic transitions that span about 150 K, with Curie temperature ranging from 230 K for equiatomic VFeCoNiCu to 736 K for non-equiatomic $V_{0.25}$FeCoNi$Cu_{1.75}$. The magnetic properties of the V-Fe-Co-Ni-Cu compounds were evaluated by means of density functional theory. Individual element-specific moments, magnetic exchange integrals between atomic pairs, and Curie temperatures were calculated. $V_{0.85}$FeCoNi$Cu_{1.15}$ is selected due to its Curie temperature of 329 K, and its calculated isothermal entropy change of 0.75 J/kg·K for a field change of 5 T is comparable to other 3d metal-based high entropy alloys that form disordered solid solutions.

© 2022 The Author(s). Published by Elsevier B.V.
CC_BY_4.0

1. Introduction

As climate change tends to raise average temperatures and increases the occurrence of temperature anomalies, cooling and heating of common areas will play a crucial role in future worldwide energy demand [1,2]. In that regard, more efficient technologies will allow for lower stress on energy grids. Amongst the more promising alternatives to current domestic vapor compression technologies for refrigeration or air conditioning solutions, magnetocaloric devices stand out, as they use less environmentally deleterious substances whilst providing better efficiency during thermal cycling [3,4]. At the core of these devices are materials that heat or cool due to changes in their internal magnetizations; they are called magnetocaloric materials. The most common properties used to measure the intensity of the magnetocaloric effect in a compound for a given magnetic field, are the adiabatic temperature change (dT_{ad}) and the isothermal entropy change (ΔS_m) [5,6]. The former can be obtained directly from specialized devices measuring the compound's temperature during a near-adiabatic magnetization/demagnetization cycle, while the latter can be calculated indirectly by magnetization measurements across a magnetic transition temperature, such as the Curie temperature (T_C) in ferromagnetic (FM) systems, by adaptation of a Maxwell relation:

$$\Delta S_m = \mu_0 \int_{H_i}^{H_f} \left(\frac{\partial M}{\partial T}\right)_H . \quad (1)$$

Here, μ_0 is the vacuum permeability constant, H_i and H_f are the minimum and maximum applied magnetic fields, and $\left(\frac{\partial M}{\partial T}\right)_H$ denotes the derivative of mass magnetization with respect to temperature

* Corresponding author.
E-mail address: christoph.frommen@ife.no (C. Frommen).

https://doi.org/10.1016/j.jallcom.2022.166040
0925-8388/© 2022 The Author(s). Published by Elsevier B.V.
CC_BY_4.0

under a constant magnetic field. Among the most studied magnetocaloric compound classes are $La(Fe,Si)_{13}$, Fe_2P, magnetic shape memory alloys and MM′X compounds, where M, M′ are transition metals and X is a p-block element. These materials are attractive for magnetocaloric energy conversion due to their high ΔS_m values [5–7]. Such high ΔS_m values are ascribed to their First Order Phase Transitions (FOPT), which occur either due to concurrent structural and magnetic transitions (e.g., in MM'X and magnetic shape memory alloy compounds), or during magnetoelastic phase transitions (e.g., in $La(Fe,Si)_{13}$ and Fe_2P). However, the presence of hysteresis lowers the reversibility during a FOPT and hinders the application potential of such materials [8,9]. Therefore, it is crucial to lower the hysteresis. An alternative would be to develop new compounds with Second Order Phase Transitions (SOPT), that exhibit no hysteresis, with a reasonable ΔS_m, thus exhibiting a bigger reversible effect.

In this context, a new promising alloy concept that is drawing attention are High Entropy Alloys (HEA); they are disordered solid solutions (SS) formed by four or more metallic elements in similar proportions, ranging from 5 to 35 at. % [10,11]. Given the number of possible combinations due to such boundary conditions for the compositions, a trial-and-error approach would be an arduous process. Therefore, research has focused on identifying trends in phase formation by assessing a series of thermodynamic parameters. Several of them influence the number of phases, and phase structure in such disordered solutions. MacDonald et al. argue that a configurational entropy (S_{conf}) ≥ 12.465 J/mol·K (1.5 R, where R is the universal gas constant) favours the formation of disordered SSs [12]. Besides S_{conf}, atomic size difference (δ) ≤ 6.6 % and enthalpy of mixing (ΔH_{mix}) between −15 and +5 kJ/mol are property values that are said to help stabilize SSs in HEAs [13]. Guo [14] also argues on the role of Valence Electron Concentrations (VEC), where VECs <6.87 tend to form body-centered cubic (bcc) alloys, 6.87 ≤ VECs ≤ 8 stabilize a mixture of bcc and cubic close packed (ccp) structures, and VECs > 8 fully stabilize ccp structures.

Such properties mentioned above help to provide guidelines for solid solution formation. Another method for prediction of structure and phase presence in alloys is the CALculation of PHAse Diagram (CALPHAD) method, which relies on data derived from experimental thermodynamic databases for binary and ternary alloys [15].

Investigations of HEAs were initially aimed at understanding phase formation and mechanical properties, primarily for structural applications. In recent years, their distinct electronic configurations sparked interest for applications such as hydrogen storage [16], thermoelectricity [17], and magnetism [18]. In the latter field, HEAs are explored for their soft and semi-hard properties, as their crystal structures, microstructures and electronic configurations can be easily modified towards the desired properties [19]. As candidates for magnetocaloric materials, HEAs based on 3d ferromagnetic transition metal elements could have great advantages, as they feature good chemical stability, high ductility, and could easily be processed into different shapes [20,21]. However, the lack of solubility between certain elements, varying degrees of short range ordering and ultimately a low ΔS_m have so far prevented HEAs from becoming serious candidates for magnetic cooling applications [22–24].

A combined approach employing computational and experimental methods is advantageous for identifying new combinations of metallic elements that may yield the desired (micro)structure and magnetic properties. In this respect, a thorough understanding of the microstructural features of HEAs is crucial. While monophasic alloys were initially sought after, reports on multiphasic HEA systems have been showcasing a strong interplay between different phases, that can yield unexpected beneficial magnetic and mechanical properties [25–28].

To adjust the Curie temperature (T_C) towards room temperature (RT) in alloys based on ferromagnetic transition metals, elements that create antiferromagnetic exchange interactions are used. Recent explorations include melt-spun MnFeCoNiCu and heat-treated CrFeCoNiAl, which employ mainly Mn and Cr, respectively to decrease T_C [29,30].

In contrast, little attention has been given to V-containing HEAs. V can also induce antiferromagnetic interactions with Fe/Co/Ni, which lower T_C to RT. In addition, little is known about its influence on the properties, structure and microstructure of Fe/Co/Ni-based HEAs to be used as magnetocaloric materials. Thus, the potential of V-containing HEAs remains unexplored. To bridge this knowledge gap, we present experimental and computational results regarding phase formation, (micro)structure, and magnetism for two different V-containing alloy systems: $V_{1-x}FeCoNiAl_{1+x}$ and $V_{1-x}FeCoNiCu_{1+x}$ ($0 \leq x \leq 0.75$), with Al or Cu as fifth elements. Cu and Al are employed in this study as they are abundant elements, that enable the formation of solid solutions by raising S_{conf} while having very distinct number of valence electrons, which modify the VEC. They also dilute the magnetic moments in the solid solutions, aiding in lowering T_c towards RT. These systems are chosen as the equimolar compositions feature suitable ΔH_{mix}, δ and VEC values to form SSs. We study the influence of composition on magnetic ordering temperatures and magnetic exchange interactions. This is achieved by a systematic variation of the V/Al and V/Cu ratios while retaining a content of 20 at. % for Fe, Co, and Ni each (60 at. % in total). The experimental results are complemented by CALPHAD modelling and density functional theory (DFT) to elucidate structural and magnetic properties in the studied alloys.

2. Materials and methods

Metallic powders of Fe, Ni, Co, V, Cu and Al of 99.9 % purity were weighed, mixed and arc melted in a Ti-gettered home-built arc melter in argon atmosphere. The samples were remelted and turned 5 times to ensure homogeneity. Nominal compositions are described in Table 1. Phase presence and constitution were predicted by the CALPHAD method implemented by the Thermocalc 2021 software in combination with the TCHEA3 high entropy alloy database package. Property diagrams were obtained by considering all the possible phases, including intermetallic and intermediate compounds formed by the constituent elements.

Table 1
Selected properties for a series of V-Fe-Co-Ni-(Al/Cu) HEAs: configurational entropy (S_{conf}), atomic size difference (δ), enthalpy of mixing (ΔH_{mix}), and Valence Electron Concentration (VEC). The table also displays the refined lattice parameters (a) and standard deviations (σ) in brackets.

Composition	S_{conf} (J/mol·K)	δ (%)	ΔH_{mix} (kJ/mol)	VEC	a (σ) (Å)
$V_1FeCoNiAl_1$	13.38	5.38	−13.87	7.0	2.881(1)
$V_{0.8}FeCoNiAl_{1.2}$	13.31	5.63	−13.03	6.92	2.886(1)
$V_{0.6}FeCoNiAl_{1.4}$	13.11	5.86	−11.85	6.84	2.885(1)
$V_{0.5}FeCoNiAl_{1.5}$	12.95	5.96	−11.14	6.8	2.884(2)
$V_{0.25}FeCoNiAl_{1.75}$	12.33	6.21	−8.96	6.7	2.8815(3)
$V_1FeCoNiCu_1$	13.38	2.88	−1.28	8.6	3.6108(9)
$V_{0.85}FeCoNiCu_{1.15}$	13.34	2.72	0.32	8.78	3.604(1)
$V_{0.8}FeCoNiCu_{1.2}$	13.31	2.66	0.84	8.84	3.606(1)
$V_{0.6}FeCoNiCu_{1.4}$	13.11	2.4	2.92	9.08	3.601(1)
$V_{0.5}FeCoNiCu_{1.5}$	12.95	2.25	3.93	9.2	3.5981(9)
$V_{0.25}FeCoNiCu_{1.75}$	12.33	1.79	6.38	9.5	3.5960(9)

Crystal structure characterization was carried out by a Bruker D2 Phaser Cu-Kα X-ray diffractometer (λ = 1.5406 Å) in Bragg-Brentano configuration. Rietveld refinements were done using the Fullprof Suite software [31]. Scanning electron microscopy (SEM) and energy dispersive X-ray spectroscopy (EDS) were carried out in a Hitachi SU8230 ultra-high resolution cold-field emission scanning electron microscope.

Magnetic balance measurements were done on a modified Netzsch STA 449 – F3 Jupiter thermogravimetry / differential scanning calorimetry device. Magnetic balance measurements are a valuable tool for obtaining knowledge on the magnetic transitions present in the alloys, and for the determination of trends caused by compositional variations. Furthermore, the presence of different magnetic phases can be detected by changes in slopes of descent of magnetization and/or by steps in the curves.

By applying a magnetic field in a specific configuration on a thermogravimetry analysis device, the change in internal magnetic field of the sample produces a magnetic force which adds to the weight measured by the thermobalance. As the sample is heated up during the measurement, the internal magnetic field is weakened by the thermal energy, thereby lowering the measured weight until the magnetic ordering temperature T_C is reached, and no further contribution to the weight exists. It is an indirect measurement of internal magnetization, comparable to a magnetization measurement with a small applied magnetic field. Measurements were carried out in the temperature range from 300 K to 1273 K, with heating rates of 1 or 5 K/min. Magnetic balance data was normalized with respect to mass change in the samples and plotted as a function of temperature. The mass changes were normalized since the absolute values of mass change are dependent on factors such as sample shape and mass itself, which could influence the assessment of each composition.

Magnetic measurements were carried out by either a Quantum Design Magnetic Property Measurement system or a Physical Property Measurement System. Measurements as a function of temperature were carried out in a persistent applied field of μ_0H = 0.01 Tesla (T), and temperatures ranging from 10 to 370 K. Field dependent measurements were performed at 10, 50, 250, 350 and 370 K, respectively, and applied fields in the range μ_0H = 0–5 T. Field dependent measurements for the determination of the isothermal magnetic entropy change, ΔS_m, were carried out across the magnetic transition with 10 K intervals.

Ground state magnetic properties were investigated using DFT [32,33] formulated within the Lyngby version [34] exact muffin-tin orbital method [35–39]. The chemical disorder was treated within the coherent potential approximation (CPA) [40,41]. The electrostatic correction to the single-site CPA was described using the screened impurity model with a screening parameter of 0.6. The one-electron Kohn-Sham equations were solved within the soft-core and scalar-relativistic approximations. *s*, *p*, *d* and *f* orbitals were included in the basis set. The Green's function was calculated for 16 complex energy points distributed exponentially on a semi-circular contour including states within 1.1 Ry below the Fermi level. The presented results are obtained using the local spin density approximation (LSDA) to describe the exchange correlation effects. [42,43]. For the one-center expansion of the full charge density a l^h_{max} = 8 cutoff was used. The magnetic exchange interactions were calculated within the magnetic force theorem [44] for the ferrimagnetic configuration. The calculated exchange interactions were further utilized to estimate the Curie temperature (T_C) via Monte Carlo (MC) simulations implemented within the Uppsala atomistic spin dynamics (UppASD) software [45,46]. Such simulations were performed on a 40 × 40 × 40 supercell with periodic boundary conditions. The size and direction of the magnetic moments were chosen randomly at each MC trial and 10,000 MC steps were used for equilibration followed by 50,000 steps for obtaining thermodynamic averages.

3. Results and discussion

3.1. Evaluation of the thermodynamic parameters from nominal compositions

The formation of disordered SSs in HEAs is ascribed mainly to the role of configurational entropy, where S_{conf} values ≥ 12.465 J/mol·K (1.5 *R*) help to stabilize SSs. In addition to the role of S_{conf}, properties such as δ, ΔH_{mix} and VEC are of value as important guidelines for SS formation. Table 1 summarizes thermodynamic properties of V-containing HEAs reported in literature to date. With respect to the enthalpy of mixing, ΔH_{mix}, we observe values ranging from −13.87 to +6.38 kJ/mol, thus almost all compositions have values that favor SS formation, except for $V_{0.25}FeCoNiCu_{1.75}$. As for δ, differences are small and thus also favour the formation of solid solutions. When comparing the values of S_{conf} in the two systems, we find that compounds with V content < 0.25 are below the reported guideline, while those with V ≥ 0.25 have S_{conf} large enough to be considered HEAs according to the "configurational entropy definition". By evaluating the influence of VEC it can be concluded that except for $V_{0.25}FeCoNiAl_{1.75}$, all other compositions in the V-Fe-Co-Ni-Al system could be ccp, bcc or a mixture of these structures. In the V-Fe-Co-Ni-Cu system, all compositions should be ccp. To compare the literature guideline evaluations with thermodynamic database models, the compositions are modelled in CALPHAD and their expected structure and phase presence are described in detail in the next section.

Equilibrium phases have been determined in the isopleths of phase diagram using CALPHAD, with Al and Cu substitutions as a function of V reduction, shown in Fig. 1. As can be seen from (a), the equilibrium phases present in the V-Fe-Co-Ni-Al system at RT are 2

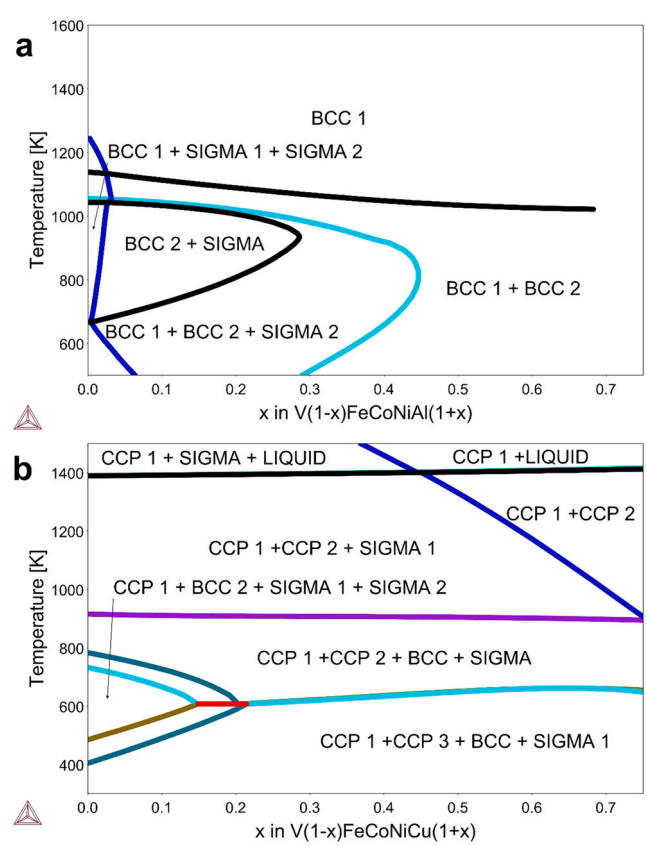

Fig. 1. Isopleth of V-Fe-Co-Ni-Al and V-Fe-Co-Ni-Cu phase diagrams, with the modifications proposed in this article produced by the CALPHAD method.

ordered bcc phases (in B2 ordering), and a sigma phase intermetallic, a tetragonal V-rich phase seen in V-rich compositions, that is not present in the predictions featuring higher Al concentrations. At temperatures above 1000 K, only one bcc phase dominates since Fe and V solubilities in the V-Fe-Co-Ni-Al main solid solution increase in equilibrium [47].

In the V-Fe-Co-Ni-Cu system, shown in Fig. 1(b), CALPHAD predicts the presence of 2 ccp phases, one bcc and one sigma phase in lower V concentrations at RT. With higher V concentrations, there is the formation of a secondary sigma phase at the expense of the ccp phase, thus forming a (ccp + bcc + sigma1 + sigma2) phase composition. At higher temperatures, the sigma phases get solubilized into a SS phase, with the formation of a secondary SS (one disordered V-Fe-Co-Ni-Cu SS and a Cu-rich phase). This secondary ccp phase is present up to 1400 K, at which point it is liquified. In summary, the CALPHAD method provides a more detailed picture of the system after the initial evaluation based on thermodynamic properties. To assess the phases, present in the as-cast V-containing alloys, we turn our attention to the analysis of their crystal structure and microstructure using X-ray diffraction and scanning electron microscopy, respectively.

3.2. Crystal structure and microstructure

The V-Fe-Co-Ni-Al alloys were brittle in the as-cast state, thus for the X-ray diffraction (XRD) measurements the samples were pulverized with a mortar and pestle. The patterns are shown in Fig. 2a. For all samples, the diffraction data could be indexed as disordered bcc or ordered B2 alloys, as indicated by the (100) reflection around $2\theta = 30^{o}$. The respective lattice parameters are given in Table 1. Except for the V-Fe-Co-Ni-Al equiatomic composition, the non-equiatomic compositions follow a trend towards smaller lattice constants, when the V content is lowered. Note, that the higher Al compositions (up to the $V_{0.25}FeCoNiAl_{1.75}$ composition) result in B2-ordered phase with clearly visible (100) superstructure reflections, corresponding to the end of the phase diagram seen in Fig. 1a. In this B2 ordering, symmetry is lowered towards the *Pm*-3*m* space group. Thus certain atoms remain in specific positions, modifying the structure factors influencing the diffraction pattern. The structure factors with the best description of the patterns occur when 1a positions are taken by V, Al and half of the Fe, whereas the remaining Fe, Co and Ni atoms occupy the 1b position [48].

To gain insight into the phase and element distribution after the solidification process for the as-cast V-containing alloys, SEM imaging and EDS were carried out on $V_{0.8}FeCoNiAl_{1.2}$ and $V_{0.85}FeCoNiCu_{1.15}$. For compositions containing Al, the data shows a dendritic microstructure, see Fig. 2b. The composition measured with EDS in dendritic (clear) and interdendritic (dark) areas are displayed in Table 2, with no clear formation of secondary phases.

Dendritic and interdendritic areas display very different compositions, which can be attributed to constitutional supercooling. This phenomenon occurs during cooling of alloys when local solubility differences at solid/liquid interfaces result in a liquid that is poorer in certain elements. This creates an undercooling effect, leading to the formation of compositional gradients between dendritic (first solidification product) and interdendritic areas (solute-poor liquids that solidify in a later stage). In the V-Fe-Co-Ni-Al alloys, constitutional supercooling acts to form dendritic areas richer in Ni,

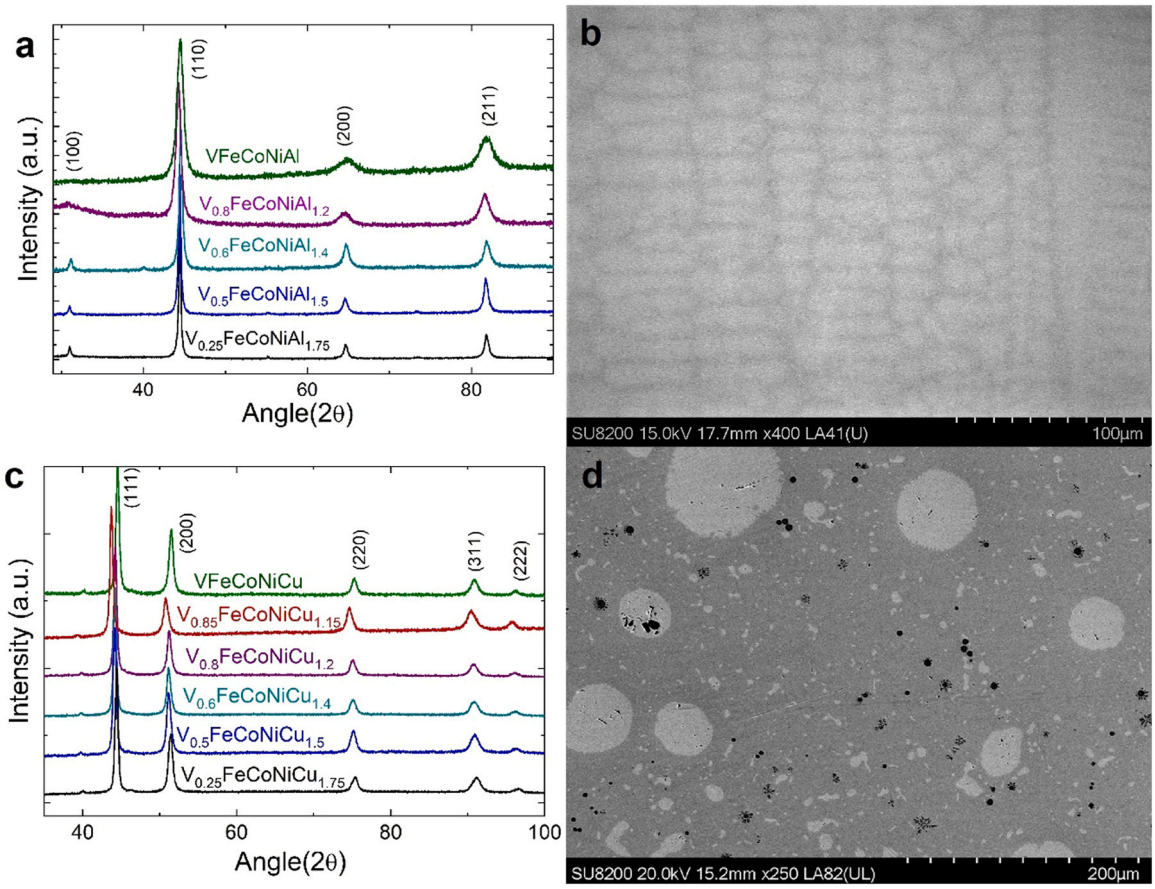

Fig. 2. a) XRD patterns for a series of V-Fe-Co-Ni-Al high entropy alloys (Cu Kα; λ = 1.5406 Å); b) SEM image in Back-scattered mode for $V_{0.8}FeCoNiAl_{1.2}$ displaying a dendritic microstructure; c) XRD patterns for a series of V-Fe-Co-Ni-Cu compounds (Cu Kα; λ = 1.5406 Å); d) SEM image in Backscattered Electron mode for $V_{0.8}FeCoNiCu_{1.2}$ exhibiting the main SS in gray, the Cu-rich phase in clear regions and the areas in black where the sigma intermetallic phase was precipitated and removed during preparation.

Table 2
Composition of dendritic areas, interdendritic areas, and the average composition measured in $V_{0.8}FeCoNiAl_{1.2}$ as determined by EDS. As a comparison, the nominal composition is displayed as well.

Element	Dendrite (%)	Interdendrite (%)	Average (%)	Nominal (%)
Fe	17.2 ± 0.8	24.0 ± 2.3	20.6 ± 3.8	20
Co	21.8 ± 0.2	21.0 ± 0.1	21.4 ± 0.4	20
Ni	22.2 ± 0.4	18.8 ± 0.9	20.5 ± 1.9	20
V	12.4 ± 0.6	18.1 ± 1.9	15.3 ± 3.2	16
Al	26.3 ± 0.9	18.0 ± 3.4	22.1 ± 4.8	24

Co and Al, with a higher solidification temperature, and interdendrites richer in Fe and V in $V_{0.8}FeCoNiAl_{1.2}$which solidify later. The trend of Fe and V to be expelled from an early solidification front at lower temperatures is also proposed by CALPHAD as V and Fe tend to form a secondary bcc phase at lower temperatures (see Fig. 1a).

The V-Fe-Co-Ni-Cu HEAs were ductile, so the alloys were filed into fine powders. XRD patterns are shown in Fig. 2c. V-Fe-Co-Ni-Cu alloys display only ccp reflections in their as-cast state with no signs of ordering. Note, that due to a different sample height, a different sample displacement factor occurs in the $V_{0.85}FeCoNiCu_{1.15}$ sample, thus shifting its diffraction pattern slightly to the left. An example of the Rietveld refinement performed for $V_{0.85}FeCoNiCu_{1.15}$ is seen in Fig. 3a. The observed reflection peaks evidence shifts from their expected positions, as well as broadening that cannot be modeled by FWHM Caglioti function or strain contributions described by regular Pseudo-Voigt profile functions. Instead, it is concluded that this is the result of stacking faults. Stacking faults in HEAs are quite common as a higher number of elements tend to reduce the stacking fault energy [49–51]. To correctly describe the influence of stacking faults in the diffraction pattern, the FAULTS program was used. FAULTS employs a Levenberg–Marquardt algorithm to model stacking faults and is part of the Fullprof suite. It is based itself on the DIFFaX program which computes diffraction from layered crystals that contain stacking faults [52]. The best fit to the data with FAULTS for $V_{0.85}FeCoNiCu_{1.15}$ is presented in Fig. 3a. The difference in the (200) peak position for a perfectly stacked ccp lattice, and one featuring stacking faults is exemplified in Fig. 3b. Note the improved peak shift description for the FAULTS refinement compared to Fullprof, which is obtained by employing a mixture of intrinsic and extrinsic stacking faults, in a ratio between 50 % and 65 % intrinsic stacking faults, with stacking faults present from 6 % to 9 % of the ccp planes.

The lattice parameters in $V_{1-x}FeCoNiCu_{1+x}$ are lower with reduced V content, since Cu has smaller radius than V (see Table 1) [11]. The SEM micrograph for $V_{0.85}FeCoNiCu_{1.15}$ in Fig. 2d obtained in backscattered electron mode evidences two SS phases. During later stages of sample preparation, a third phase is removed from the matrix. During grinding and polishing, the surface of the sample is submitted to high stress locally. In the case of microstructures

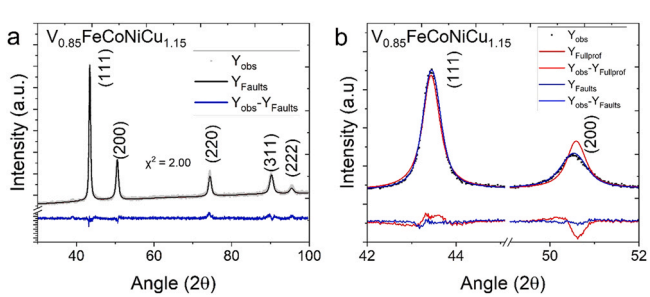

Fig. 3. a) Rietveld refinements of $V_{0.85}FeCoNiCu_{1.15}$ XRD pattern performed with the FAULTS program. b) comparison between the refinement with and without stacking faults performed with FAULTS and Fullprof, respectively. Observed intensities as dots, refined intensities as coloured lines, and difference plots on the bottom of each graph.

featuring brittle phases or low coherence between the phases, some areas can be pulled out of the microstructure. Therefore, to gain insight about this phase, the chemical composition was determined by EDS during the intermediate stages of metallographic preparation. The results point towards the sigma phase, commonly formed between V, Fe, Co, Ni and Cu in HEAs [53]. Table 3 lists the compositions of different phases present in $V_{0.85}FeCoNiCu_{1.15}$, together with their average measured composition as determined by EDS and the nominal composition.

The main phase is a SS that is poor in copper (12.7 at. %) but retains most of the ferromagnetic transition metals and V. The remaining Cu segregates into a secondary phase, whose formation can be ascribed to a lack of solubility of Cu in the main SS with V-Fe-Co-Ni-Cu. A subsequent diffusion of Fe, Co and Ni during cooling into the Cu-rich phase is also observed. Possible reasons for the poor solubility of Cu in the matrix can be related to an immiscibility between Cu and V, or low solubility of Cu with Fe and Co [24,47,54]. Despite the presence of a Cu-rich phase in the micrographs, the diffraction patterns of the V-Fe-Co-Ni-Cu samples appear to be monophasic. As the Cu-rich phase exhibits a ccp structure whose atoms are very similar in size to the main SS (Cu has atomic radius comparable to Fe, Co and Ni), the diffraction patterns for these two phases would show a significant overlap, especially considering peak broadening effects associated with lattice distortions in as-cast HEAs. The present findings illustrate, why complementary techniques such as XRD and SEM are needed to fully describe the phase content, structure, and microstructure in HEAs.

When evaluating the role of the literature parameters (S_{conf}, δ, ΔH_{mix} and VEC), one can conclude that they enable early screening of SS compositions. Both systems contain SSs as majority phases: a monophasic bcc SS in the case of V-Fe-Co-Ni-Al alloys, and two ccp SSs in the V-Fe-Co-Ni-Cu system. It is important to highlight some specific property correlations, such as $\Delta H_{mix}$and δ for instance, which can be used together to determine mono and multiphasic solid solution fields [13,14]. VEC is also a relevant descriptor of possible structures in HEAs [14].

Nevertheless, they cannot be taken as the sole descriptors for phase presence and structure in HEAs. The S_{conf} property value used in the HEA literature assumes a completely random SS and neglects the possibility of a SS with a non-random distribution (sub-regular type solution). This is the dominant case in binary metallic systems [55]. The determination of S_{conf} in such sub-regular systems is not easily performed. Likewise, the Miedema model, commonly used for the determination of ΔH_{mix}, is also only accurate in certain systems as it assumes liquid mixing of the binaries, not solid ones [11,56]. Their role is, therefore, mainly to guide the early composition screening.

The experimentally observed phases at RT are also different from the ones predicted by CALPHAD. Instead, the samples are very similar to the phase content seen in the CALPHAD predictions in temperatures above 1000 K. This is caused by the metastability of the as-cast HEAs. As-cast samples withstand cooling rates of hundreds of degrees per second inside the Cu hearth during arc melting, enabling a metastable state. In this condition, only phases with a high thermal activation are formed, which are still present during the cooling process. At lower temperatures, thermodynamic equilibrium cannot be reached due to the lack of diffusivity during regular solidification processes.

In practical terms, this means that only phases seen in as-cast V-Fe-Co-Ni-Al and V-Fe-Co-Ni-Cu are phases present in diffusion active temperatures, above 1000 K. In summary, for the present HEAs in equilibrium, the literature parameters are a first step for determination of possible solid solutions, and in a subsequent step the CALPHAD method provides accurate information of phase presence. Therefore, CALPHAD can be considered as a valuable tool for the prediction of phases in multicomponent alloys.

Table 3
Composition of main SS and Cu-rich SS phases in $V_{0.85}FeCoNiCu_{1.15}$, as well as the average composition for the alloy as determined by EDS. Nominal composition shown for comparison.

Element	Main SS (%)	Cu-rich SS (%)	Sigma (%)	Average (%)	Nominal (%)
Fe	22.5 ± 0.6	2.5 ± 0.3	14.5 ± 1.4	18.3 ± 0.3	20
Co	24.1 ± 0.2	1.9 ± 0.3	15.1 ± 1.2	21.4 ± 0.4	20
Ni	22.8 ± 0.6	6.4 ± 0.2	13.7 ± 1.2	22.8 ± 0.2	20
V	17.9 ± 2.0	0.3 ± 0.1	48.3 ± 3.4	15.0 ± 0.7	17
Cu	12.7 ± 0.5	88.9 ± 0.3	8.4 ± 1.4	22.5 ± 1.5	23

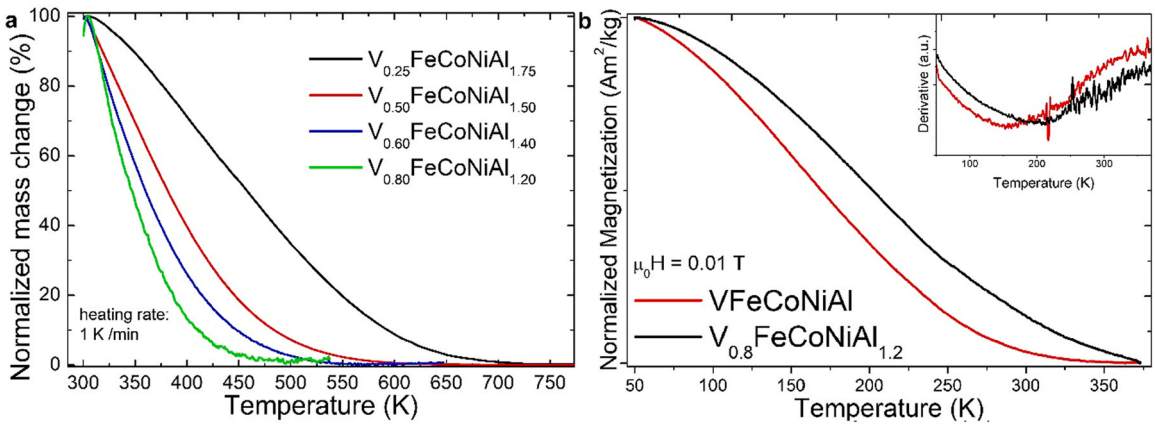

Fig. 4. (a) Indirect magnetization from magnetic balance measurements; (b) magnetization as a function of temperature for the $V_{1-x}FeCoNiAl_{1+x}$ system.

3.3. Establishment of composition trends: magnetic balance and magnetic characterization

The $V_{1-x}FeCoNiAl_{1+x}$ as-cast samples feature a broad transition, spanning more than 300 K, as seen from the magnetic balance measurements in Fig. 4a. The $V_{0.25}FeCoNiAl_{1.75}$ sample is the only composition where magnetization reduction begins above RT, spanning from 300 to 723 K. In other compositions studied, it was not possible to infer where the reduction in magnetization begins, i.e., where the transition begins. The normalized curves in Fig. 4a feature different slopes. This can be a sign of inhomogeneities modifying local average exchange interactions and the local T_C values, and then change the slope of the curves. To determine the behaviour in some compositions below RT, thermomagnetic measurements were performed for VFeCoNiAl and $V_{0.8}FeCoNiAl_{1.2}$, see Fig. 4b. Curves were normalized in order to ease visualization. Absolute magnetization values at different temperatures are better displayed in field-dependent measurements seen in Fig. 6a.

Both equimolar and $V_{0.8}FeCoNiAl_{1.2}$ samples feature the same behavior seen in magnetic balance measurements with broad transitions spanning more than 300 K. As expected, samples with higher V content have their transitions shifted towards lower temperatures. The T_c values are determined from the derivative values of magnetization as a function of temperature, see the inset of Fig. 4b for VFeCoNiAl and $V_{0.8}FeCoNiAl_{1.2}$, respectively. For VFeCoNiAl, $V_{0.8}FeCoNiAl_{1.2}$ and $V_{0.25}FeCoNiAl_{1.75}$, T_C values were determined as 155, 200 and 456 K, respectively. Compositions featuring transitions above or below the equipment's temperature threshold did not have their T_C measured, as it was not possible to capture the full extent of the transition.

This continuous decrease of magnetization as a function of temperature is further evidenced in field-dependent magnetization M(H) measurements shown in Fig. 6a for the equimolar VFeCoNiAl composition. The saturation magnetization (M_S) drops with temperature, from 38 Am^2/kg at 10 K to around 5 Am^2/kg at 370 K. The magnetization shows a linear increase at higher fields, indicating a possible PM contribution to the ferromagnetic signal.

The magnetic balance measurements for the $V_{1-x}FeCoNiCu_{1+x}$ as-cast alloys, shown in Fig. 5a, feature narrower magnetic transitions compared to the V-Fe-Co-Ni-Al samples, spanning only around

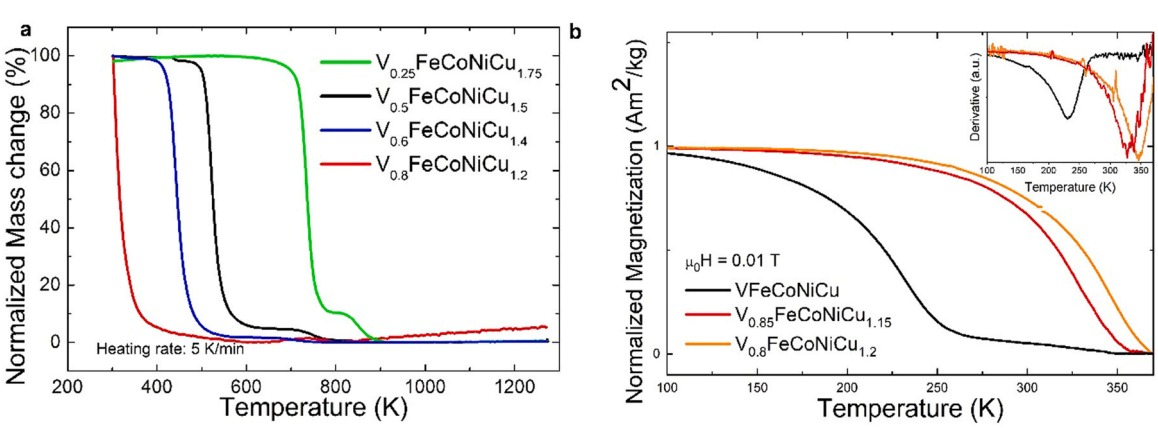

Fig. 5. (a) Indirect magnetization from magnetic balance measurements; (b) magnetization as a function of temperature for the $V_{1-x}FeCoNiCu_{1+x}$ system.

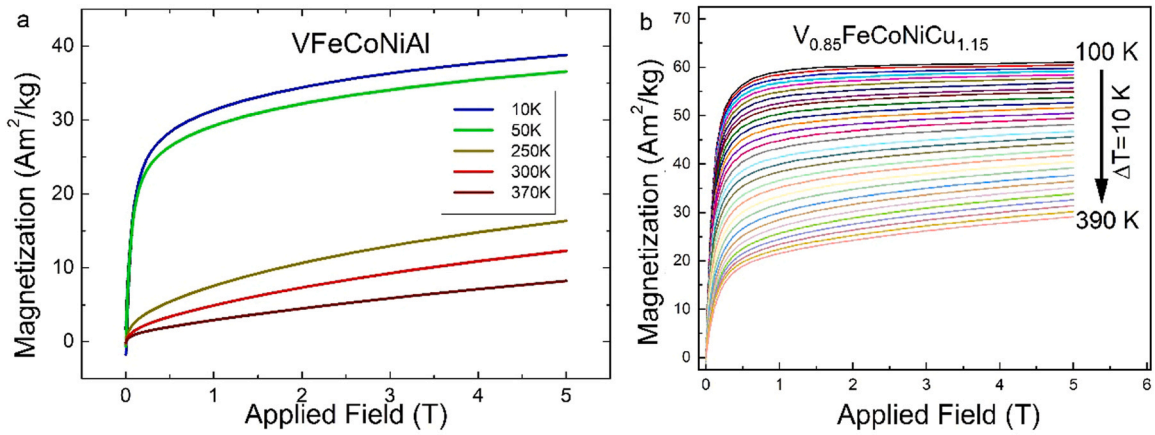

Fig. 6. Magnetization as a function of applied field for (a) VFeCoNiAl and (b) $V_{0.85}FeCoNiCu_{1.15}$.

150 K. Similar to the V-Fe-Co-Ni-Al samples, a reduction in V content and increase in the fifth element content (Cu) raises T_C to higher temperatures. Note, that the onset of the magnetic transition for the $V_{0.8}FeCoNiCu_{1.2}$ sample lies below RT (outside our measurement range). It is therefore not possible to correctly evaluate its transition temperature by the magnetic balance measurements. It can be concluded that samples containing 16 at. % V or more feature part of their magnetic transitions around RT and below. Therefore, additional temperature-dependent magnetization measurements were performed. Fig. 5b shows the normalized magnetization obtained for three samples: $V_{1-x}FeCoNiCu_{1+x}$ (x = 0.0, 0.15 and 0.2) measured between 100 K and 400 K in an external field of 0.01 T. The insert in Fig. 5b shows the derivative of magnetization as a function of temperature and is used to determine T_C.

Experimental T_C values for the V-Fe-Co-Ni-Cu samples are shown in Table 4. A secondary step or a slight slope shift after the main magnetization decrease is observed, which evidences the presence of a secondary magnetic phase both in high and low temperature measurements. This response can be attributed to the secondary Cu-rich phase, with small concentration of FM 3d elements. As the magnetocaloric effect in such SOPT is directly related to the sharpness of the magnetic transition, it is possible to conclude that the V-Fe-Co-Ni-Cu system is more promising for magnetocaloric applications than the V-Fe-Co-Ni-Al system under the current conditions. To shed more light on the role of each element on the magnetic properties of $V_{1-x}FeCoNiCu_{1+x}$ alloys, DFT calculations were performed.

The total and element resolved magnetic moments of $V_{1-x}FeCoNiCu_{1+x}$ alloys as a function of V and Cu concentrations are listed in Table 4 in units of Bohr magnetons, μ_B. We can observe that the total magnetic moment per unit cell m_{tot} increases from 0.59 μ_B for the equiatomic alloy to 0.82 μ_B for $V_{0.25}FeCoNiCu_{1.75}$. This can be attributed to the change of the element resolved magnetic moments with V and Cu concentration. Fe, Co and Ni couple parallel to each other in all alloys and their moments increase with increasing Cu content. This is in line with the slight re-population of the 3d orbitals plotted in Fig. 7 due to a relative change in V/Cu concentration. It increases the population of the spin-up channel and decreases the population of the spin-down channel as observed for Fe, Co and Ni in $V_{0.25}FeCoNiCu_{1.75}$, compared with spin channel occupations in $V_1FeCoNiCu_1$. Due to a hybridisation of the 3d orbitals of V and Cu with the 3d orbitals of Fe, Co and Ni, induced magnetic moments appear on V as well as on Cu. While the magnetic moment on Cu is small and couples parallel to the moments of Fe, Co and Ni, the magnetic moment developed on V is larger and antiparallel to the rest of the moments. The small magnitude of m_{Cu} is due to the fully filled 3d-orbitals as presented in Fig. 7, which is a direct consequence of the *sd*-hybridisation present in Cu. In contrast, V has a less than half-filled 3d orbital and therefore a large number of states at the Fermi energy (see Fig. 7). This makes V to be easily polarised and results in a moment of −0.48 μ_B, for $V_1FeCoNiCu_1$ which increases to −0.93 μ_B, for $V_{0.25}FeCoNiCu_{1.75}$. This increase of the magnetic moment is a consequence of the migration of the spin-up electrons into the spin-down channel. We then proceed to estimate T_C and compare it to the experimental values.

The calculated T_C values are increasing with decreasing V concentration, from 220 K for the equiatomic alloy to 520 K for $V_{0.25}FeCoNiCu_{1.75}$, as shown in Table 4. This agrees with experimental findings and is a consequence of the dilution of V in the SS [39]. The calculated Curie temperatures in Table 4 are consistently lower than the measured ones, and the difference increases with decreasing vanadium content, from 10 K for the equiatomic alloy to 216 K for $V_{0.25}FeCoNiCu_{1.75}$. Results presented here are obtained using LSDA, that is regarded as giving the lower bound for the values describing the magnetic properties. The generalized gradient approximations, for example the Perdew-Burke-Ernzerhof exchange-correlation functional [57], gives larger values for calculated magnetization and estimated Curie temperatures. For the investigated alloys, we observe a 1.2 % constant shift towards higher moments and T_C for each composition, and therefore the slope for the Tc variation with V/Cu concentration is not affected. Two factors may account for this discrepancy: (1) the difference between the ideal

Table 4
Total (m_{tot}) and element resolved ($m_{element}$) magnetic moments in units of Bohr magnetons, μ_B, calculated and experimental Curie temperatures (T_C) in K for a series of $V_{1-x}FeCoNiCu_{1+x}$ alloys.

Composition	$m_{tot}(\mu_B)$	$m_V(\mu_B)$	$m_{Fe}(\mu_B)$	$m_{Co}(\mu_B)$	$m_{Ni}(\mu_B)$	$m_{Cu}(\mu_B)$	calc. T_C (K)	exp. T_C (K)
$V_1FeCoNiCu_1$	0.59	-0.48	2.10	1.07	0.23	0.01	220	230
$V_{0.85}FeCoNiCu_{1.15}$	0.62	-0.53	2.17	1.14	0.26	0.01	260	329
$V_{0.8}FeCoNiCu_{1.2}$	0.64	-0.56	2.20	1.17	0.27	0.01	290	345
$V_{0.6}FeCoNiCu_{1.4}$	0.70	-0.67	2.29	1.27	0.31	0.01	360	440
$V_{0.5}FeCoNiCu_{1.5}$	0.73	-0.73	2.34	1.31	0.33	0.01	400	521
$V_{0.25}FeCoNiCu_{1.75}$	0.82	-0.93	2.46	1.43	0.40	0.02	520	736

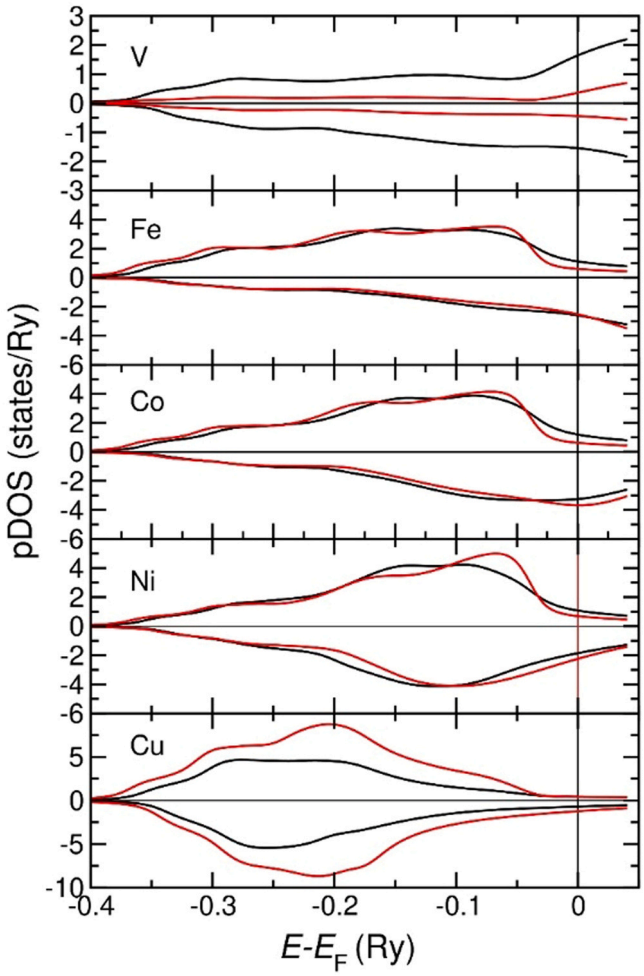

Fig. 7. Element resolved density of states. Black lines represent VFeCoNiCu and red lines represent $V_{0.25}FeCoNiCu_{1.75}$. Density of states are weighted with the concentration of each element.

equilibrium alloys modelled by the theory and the multi-phase experimental samples. The change in V/Cu ratio affects the phase ratio between the main SS, Cu-rich SS and sigma-phase. This in turn modifies the composition of the main SS, further diverging from the nominal composition. The model also does not take into account the influence of defects i.e. local composition variations, local lattice relaxations, vacancies, stacking faults, etc.; (2) temperature-induced longitudinal fluctuations of the magnetic moments are not accounted for, even though they are important to properly describe high temperature magnetism of 3d alloys [34]. However, while the above-mentioned factors may be important, the trend in the T_C variation with concentration is well captured without taking them into account. Therefore, the complex description of high temperature magnetism and the effect of structural complexity on the magnetic properties of these alloys are left to another study.

Field dependent measurements were carried out with an applied field of μ_0H = 0–5 T at selected temperatures between 10 K and 390 K in $V_{0.85}FeCoNiCu_{1.15}$, and are displayed in Fig. 6b. The magnetization as a function of applied field for the V-Fe-Co-Ni-Cu samples is different from the V-Fe-Co-Ni-Al sample shown in Fig. 6a, as purely FM behaviour is seen in the measurements at 10 K. This is evidenced by a plateau at high magnetic fields, i.e., the sample reaches its saturation magnetization, M_s. In the isothermal measurements performed at higher temperatures, magnetization displays a more paramagnetic character, as magnetization begins to increase linearly with the applied field. Note the presence of a

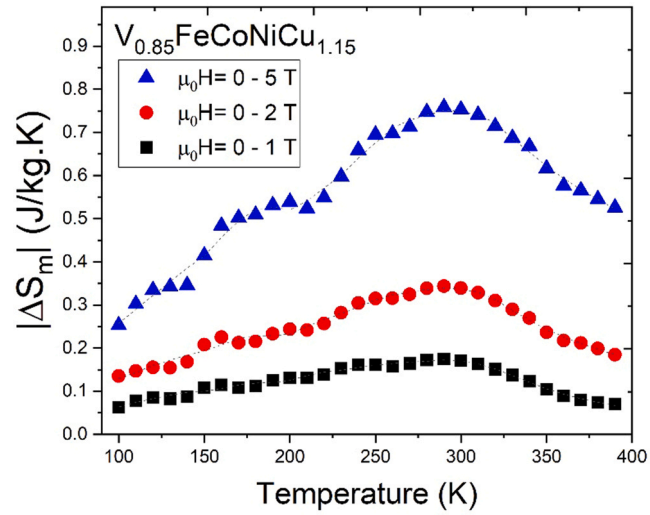

Fig. 8. Isothermal magnetic entropy change for $V_{0.85}$ $FeCoNiCu_{1.15}$ between 100 and 390 K.

secondary ferromagnetic phase in the M(H) curves as well, as some magnetization is retained at 390 K. Saturation magnetization values for $V_{0.85}FeCoNiCu_{1.15}$ are higher than for the 5-element equiatomic alloy with Al; with M_s reaching up to 61 Am^2/kg at 100 K, to approximately 29 Am^2/kg at 390 K. We attribute this to the presence of the secondary phase with higher M_s.

3.4. $V_{0.85}FeCoNiCu_{1.15}$ magnetocaloric properties and magnetic system description

From the field dependent data shown previously, one can indirectly obtain ΔS_m from Eq. 1 between 100 and 390 K, and the results are shown in Fig. 8 for field changes of 0–1, 0–2 and 0–5 T, respectively. The whole transition from the main SS phase branches over this wide temperature range, peaking around RT (the biggest values are seen at T = 290 K). The maximum values are approximately 0.15, 0.3 and 0.75 J/kg.K for the 0–1, 0–2 and 0–5 T changes, respectively. Even though at higher temperatures a complete paramagnetic state is not yet reached (as seen by the remaining magnetization in the field dependent magnetization curves in Fig. 6b), most of the sample has transitioned, leading to smaller ΔS_m values after the peak around RT. Small variations between each temperature step can be seen that gives small deviations throughout the temperature range, which stems from a non-normalized microstructure with compositional variations across the main SS phase. However, the trend of the transition can be clearly seen across the studied temperature range. A similar behavior of ΔS_m variations between temperature steps is seen in as-cast $Mn_{0.89}Cr_{0.3}Fe_{0.5}Co_{0.2}Ni_{0.5}Al_{0.3}$ HEA where despite these variations, the behavior of the transition is captured [20,58].

This influences the dM/dT values, which in turn causes a gradual decrease of the ΔS_mcurve, as seen from Eq. (1). The highest value of 0.75 J/kg.K for a field change of 5 T is comparable to what has been reported for ccp HEAs featuring a SOPT, such as Cr-containing $CrFeCoNiPd_x$ and $CrFeCoNiAl_x$ [20,59]. Nevertheless, the value is lower than the $Mn_{27}Cr_7Ni_{33}Ge_{25}Si_8$ SOPT HEA and $Mn_{22}Fe_{22}Ni_{22}Ge_{17}Si_{17}$ FOPT HEA, which are modifications of the MM'X alloy systems containing hexagonal or orthorhombic structures [60,61]. In order to gain a better understanding of the magnetic order in the as-cast V-Fe-Co-Ni-Cu alloys, pair exchange integrals (J_{ij}) were calculated by means of DFT.

In metals featuring SOPTs, ΔS_m values arise from the demagnetization of the magnetic moments from direct exchange interactions

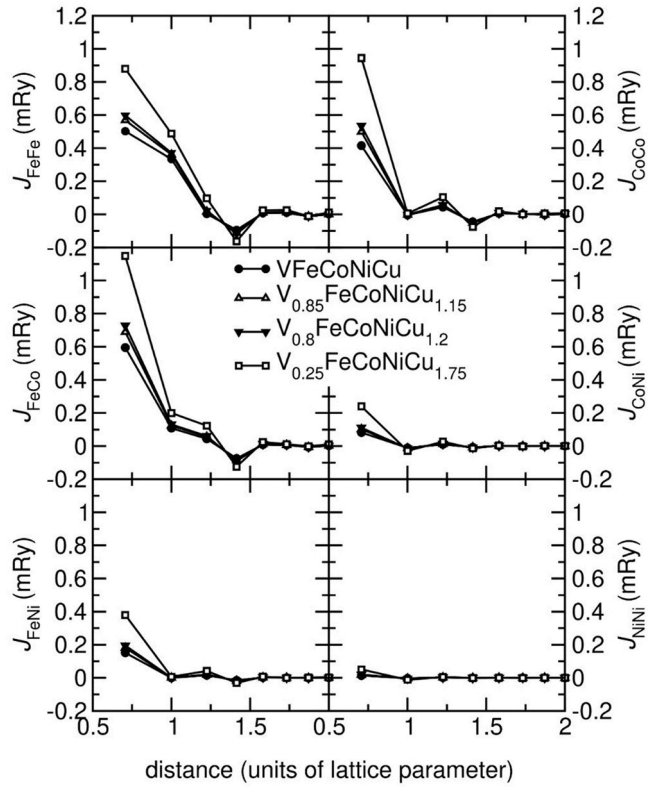

Fig. 9. Magnetic exchange integrals between the magnetic elements Fe, Co and Ni as a function of atomic distance for a series of $V_{1-x}FeCoNiCu_{1+x}$ (x = 0, 0.15, 0.2, and 0.75) samples.

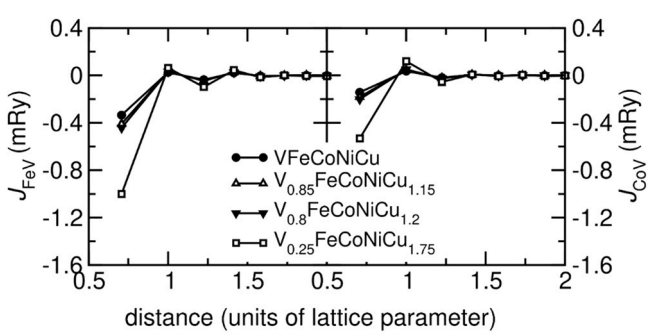

Fig. 10. Magnetic exchange integrals between Fe and V, and Co and V, respectively, as a function of atomic distance for a series of $V_{1-x}FeCoNiCu_{1+x}$ (x = 0, 0.15, 0.2, and 0.75) samples.

between the atom pairs at T_C. To describe the V-Fe-Co-Ni-Cu system, the calculated magnetic exchange integrals are plotted in Figs. 9 and 10. A general observation is that the exchange integrals show an oscillatory behaviour with distance and decay after about 1.5 lattice parameter units (5th coordination shell). Also, all interactions increase with decreasing V content. The strongest FM couplings can be found between the magnetic elements Fe and Co, i.e., J_{FeFe}, J_{FeCo} and J_{CoCo} (see Fig. 9). They become stronger with decreasing V concentration, which is in line with the increase of local magnetic moments of these elements. Since Ni possesses only a small magnetic moment, it also shows a weaker FM coupling with itself and with Fe and Co (see Fig. 9 for J_{FeNi}, J_{CoNi} and J_{NiNi}).

The magnetic coupling between Cu, V, and the magnetic elements as well as for Cu-Cu, Cu-V and V-V pairs is negligible and therefore not shown. However, we find a large negative nearest neighbour coupling for Fe and Co with V (see Fig. 10) that increases with decreasing V content that becomes comparable in size to the J_{FeFe}, J_{FeCo} and J_{CoCo} exchange integrals for $V_{0.25}FeCoNiCu_{1.75}$.

In disordered materials such as HEAs, the high number of possible parallel and antiparallel magnetic couplings surrounding each element creates different magnetic configurations in neighbouring coordination shells. This leads to a distribution of exchange interactions and consequently magnetic ordering temperatures that result in broad magnetic transitions that span a large range of temperatures. This behaviour may be further complicated by non-normalized microstructures common in regular solidification processes. In them, a deviation from a random SS occurs leading to inhomogeneities or ordering. This results in micro segregation in clusters within a SS phase or in some cases, the formation of secondary phases. All of this can contribute negatively, lowering the total entropy change. This non-normalized microstructure featuring composition gradients within the SS yields a distribution of T_C values, which in turn lowers the maximum ΔS_m values. This negative influence of microstructure can be minimized by applying different processing routes, as has been reported for rapidly-solidified MnFeCoNiCu [29]. The use of processes inducing fast cooling can minimize the dwelling time in such diffusion-activated regimes, and thus reducing inhomogeneities.

On the other hand, adequate heat treatments can be employed on certain alloys to increase the change in magnetization with respect to temperature ($\frac{\partial M}{\partial T}$). By inducing the formation of intermetallics or ordered phases that enable strong ferromagnetic interactions, it is possible to modify the material and thus increase ($\frac{\partial M}{\partial T}$). In the Cr-based HEA $Cr_{0.5}FeCoNi_{0.5}Al_x$, the neighborhood of Fe changes from a disordered SS that contains Fe, Co, Ni, Cr and Al to one where Fe is precipitated into Fe-Cr nanoparticles [26,30]. This precipitate contributes ferromagnetically due to an exchange coupling with the surrounding FM Al-Ni-Co matrix. Due to this particular microstructure, ΔS_m values are higher (~0.5 J/kg.K at $\mu_o H$ = 2 T) than for HEAs that feature completely disordered structures. We believe that similar strategies can be employed to improve the characteristics of the magnetic SOPTs in the V-Fe-Co-Ni-Cu HEAs presented here.

4. Conclusions

$V_{1-x}FeCoNiAl_{1+x}$ and $V_{1-x}FeCoNiCu_{1+x}$ HEAs were explored as candidates for magnetic refrigeration applications. Compositions were chosen in agreement with well-known properties in the literature. SS phase formation guidelines based on literature results were compared with the CALPHAD method and with experimental results of the processed alloys. The alloys studied were all in an as-cast state. Compounds in the V-Fe-Co-Ni-Al system are monophasic and crystallize in a bcc lattice and tend to order themselves as B2 structures as Al content increases. The V-Fe-Co-Ni-Cu system features a main SS, a Cu-rich SS, and a V-containing intermetallic phase. Due to a limit of Cu solubility in the main SS, Cu segregates into a secondary Cu-rich phase.

The thermodynamic parameters help to establish a first evaluation of proposed V-Fe-Co-Ni-Al and V-Fe-Co-Ni-Cu HEAs before processing, thus helping to determine mono/multiphasic compositions that can yield interesting properties. The CALPHAD calculations differ from experimental results due to samples being in a metastable condition in their as-cast state. However, the predictions made from CALPHAD for phase composition and presence in diffusion activated regimes (high temperatures) is very similar to what is seen in the as-cast samples.

A substitution of V by Al or Cu raises magnetic transition temperatures for both systems. The Al-containing alloys feature a broad

magnetic transition that spans more than 400 K. They also exhibit lower magnetization change values than the Cu-containing alloys. This is attributed to the presence of paramagnetic Al and V, as well as big compositional gradients in their microstructure. The Cu-containing samples feature a magnetic transition that spans 150 K with higher magnetization value changes, which makes the V-Fe-Co-Ni-Cu alloys better candidates for magnetocaloric applications than the V-Fe-Co-Ni-Al alloys. An analysis of the magnetic exchange interactions in the V-Fe-Co-Ni-Cu alloys by means of DFT shows strong FM interactions between Fe, Co and Ni and negligible interactions between Cu-Cu, Cu-V and V-V pairs. There exists a large antiferromagnetic coupling between Fe-V and Co-V pairs that tends to lower the ferromagnetic character of the samples.

As it is known, derivatives of magnetization with temperature are an adequate indication of the magnetocaloric effect in SOPT materials; rather low derivative values for Al and Cu containing samples lead to isothermal magnetic entropy changes, ΔS_m, that are comparable to those observed in Mn- and Cr-containing HEAs. However, the values are lower when compared to the magnetocaloric effect of orthorhombic/hexagonal HEAs featuring p-block elements.

HEAs for magnetocaloric applications are typically employed in their as-cast state, which might not yield the best results. Thermomechanical treatments may change phase morphology and control metallurgical processes such as recovery, recrystallization or precipitation, which can lead to different magnetic exchange phenomena in multiphasic systems. Such possibilities are not common in rare earth intermetallics, which are typically brittle. This could lead to improved magnetocaloric properties in such versatile transition metal systems. Furthermore, the low manufacturing cost of 3d metal based HEAs compared to rare earth-based materials should make them attractive candidates for magnetocaloric energy devices.

The search for new HEA candidate materials with suitable MCE properties could be performed by a combined CALPHAD and DFT methodology. In the first step, CALPHAD calculations are performed to predict compositions of solid solutions present and possible intermetallics. In the second step, DFT calculations are employed to estimate the magnetic moments from equilibrium phases. However, only through experimental work on promising candidates will it be possible to evaluate the true performance of HEAs for magnetocaloric energy conversion.

The field of HEA research for magnetocaloric applications is still very young. The complex magnetic interactions in such disordered systems are still not completely understood, while crystal structures and microstructures depend strongly on processing conditions and are easily modifiable. The full potential of HEAs for magnetocaloric energy conversion around RT can only be reached through careful control of their elemental composition and microstructure.

CRediT authorship contribution statement

Bruno G. F. Eggert: Conceptualization, Investigation, Writing – original draft, Visualization, Writing – review & editing. Erna K. Delczeg-Czirjak: Software, Methodology, Formal analysis, Resources, Visualization, Writing – review & editing, Fernando Maccari: Investigation, Resources, Susmit Kumar: Investigation, Resources, Oliver Gutfleisch: Writing – review & editing, Resources, Helmer Fjellvåg: Writing – review & editing, Resources, Bjørn C. Hauback: Writing – review & editing, Supervision, Christoph Frommen: Writing – review & editing, Supervision, Project administration, Funding acquisition.

Data availability

Data will be made available on request.

Declaration of Competing Interest

The authors declare that they have no known competing financial interests or personal relationships that could have appeared to influence the work reported in this paper.

Acknowledgements

This work was financed by The Research Council of Norway through the NANO2021 program, Project No. 287150. E.K.D-Cz. acknowledges STandUPP and eSSENCE for financial support and the Swedish National Infrastructure for Computing (SNIC) for computational resources.

The authors acknowledge Magnus H. Sørby for fruitful discussions and his skilful assistance with structural characterization and modelling.

References

[1] C.K. Folland, T.R. Karl, M. Jim Salinger, Observed climate variability and change, Weather 57 (2002) 269–278, https://doi.org/10.1256/004316502320517353
[2] L. Cozzi, T. Gould, S. Bouckart, D. Crow, T.-Y. Kim, C. McGlade, P. Olejarnik, B. Wanner, D. Wetzel, World Energy Outlook 2020, 2050 (2020) 1–461. 〈https://www.oecd-ilibrary.org/energy/world-energy-outlook-2020_557a761b-en〉.
[3] V.K. Pecharsky, K. a Gschneidner, Giant magnetocaloric effect in Gd 5 Si 2 Ge 2, Phys. Rev. Lett. 78 (1997) 3–6, https://doi.org/10.1103/PhysRevLett.78.4494
[4] T. Gottschall, A. Gràcia-Condal, M. Fries, A. Taubel, L. Pfeuffer, L. Mañosa, A. Planes, K.P. Skokov, O. Gutfleisch, A multicaloric cooling cycle that exploits thermal hysteresis, Nat. Mater. 17 (2018) 929–934, https://doi.org/10.1038/s41563-018-0166-6
[5] O. Gutfleisch, T. Gottschall, M. Fries, D. Benke, I. Radulov, K.P. Skokov, H. Wende, M. Gruner, M. Acet, P. Entel, M. Farle, Mastering hysteresis in magnetocaloric materials, Philos. Trans. R. Soc. A Math. Phys. Eng. Sci. 374 (2016), https://doi.org/10.1098/rsta.2015.0308
[6] V. Franco, J.S. Blázquez, J.J. Ipus, J.Y. Law, L.M. Moreno-Ramírez, A. Conde, Magnetocaloric effect: From materials research to refrigeration devices, Prog. Mater. Sci. 93 (2018) 112–232, https://doi.org/10.1016/j.pmatsci.2017.10.005
[7] T. Gottschall, K.P. Skokov, M. Fries, A. Taubel, I. Radulov, F. Scheibel, D. Benke, S. Riegg, O. Gutfleisch, Making a cool choice: the materials library of magnetic refrigeration, Adv. Energy Mater. 9 (2019), https://doi.org/10.1002/aenm.201901322
[8] F. Scheibel, T. Gottschall, A. Taubel, M. Fries, K.P. Skokov, A. Terwey, W. Keune, K. Ollefs, H. Wende, M. Farle, M. Acet, O. Gutfleisch, M.E. Gruner, Hysteresis design of magnetocaloric materials—from basic mechanisms to applications, Energy Technol. 6 (2018) 1397–1428, https://doi.org/10.1002/ente.201800264
[9] T. Hess, L.M. Maier, N. Bachmann, P. Corhan, O. Schäfer-Welsen, J. Wöllenstein, K. Bartholomé, Thermal hysteresis and its impact on the efficiency of first-order caloric materials, J. Appl. Phys. 127 (2020), https://doi.org/10.1063/1.5132897
[10] R. Kozak, A. Sologubenko, W. Steurer, Single-phase high-entropy alloys - an overview, Z. Fur Krist. 230 (2015) 55–68, https://doi.org/10.1515/zkri-2014-1739
[11] D.B. Miracle, O.N. Senkov, A critical review of high entropy alloys and related concepts, Acta Mater. 122 (2017) 448–511, https://doi.org/10.1016/j.actamat.2016.08.081
[12] B.E. MacDonald, Z. Fu, B. Zheng, W. Chen, Y. Lin, F. Chen, L. Zhang, J. Ivanisenko, Y. Zhou, H. Hahn, E.J. Lavernia, Recent progress in high entropy alloy research, JOM 69 (2017) 2024–2031, https://doi.org/10.1007/s11837-017-2484-6
[13] M.C. Gao, C. Zhang, P. Gao, F. Zhang, L.Z. Ouyang, M. Widom, J.A. Hawk, Thermodynamics of concentrated solid solution alloys, Curr. Opin. Solid State Mater. Sci. 21 (2017) 238–251, https://doi.org/10.1016/j.cossms.2017.08.001
[14] Z. Wang, S. Guo, C.T. Liu, Phase selection in high-entropy alloys: from nonequilibrium to equilibrium, JOM 66 (2014) 1966–1972, https://doi.org/10.1007/s11837-014-0953-8
[15] H. Mao, H.L. Chen, Q. Chen, TCHEA1: a thermodynamic database not limited for "High Entropy", Alloy. J. Phase Equilibria Diffus 38 (2017) 353–368, https://doi.org/10.1007/s11669-017-0570-7
[16] M.M. Nygård, W.A. Sławiński, G. Ek, M.H. Sørby, M. Sahlberg, D.A. Keen, B.C. Hauback, Local order in high-entropy alloys and associated deuterides – a total scattering and Reverse Monte Carlo study, Acta Mater. 199 (2020) 504–513, https://doi.org/10.1016/j.actamat.2020.08.045
[17] H.P. Chou, Y.S. Chang, S.K. Chen, J.W. Yeh, Microstructure, thermophysical and electrical properties in AlxCoCrFeNi (0 ≤ x ≤2) high-entropy alloys, Mater. Sci. Eng. B Solid-State Mater. Adv. Technol. 163 (2009) 184–189, https://doi.org/10.1016/j.mseb.2009.05.024
[18] Q. Zhang, H. Xu, X.H. Tan, X.L. Hou, S.W. Wu, G.S. Tan, L.Y. Yu, The effects of phase constitution on magnetic and mechanical properties of FeCoNi(CuAl)x(x = 0–1.2) high-entropy alloys, J. Alloy. Compd. 693 (2017) 1061–1067, https://doi.org/10.1016/j.jallcom.2016.09.271
[19] M.C. Gao, D.B. Miracle, D. Maurice, X. Yan, Y. Zhang, J.A. Hawk, High-entropy functional materials, J. Mater. Res. 33 (2018) 3138–3155, https://doi.org/10.1557/jmr.2018.323

[20] S.M. Na, P.K. Lambert, H. Kim, J. Paglione, N.J. Jones, Thermomagnetic properties and magnetocaloric effect of FeCoNiCrAl-type high-entropy alloys, AIP Adv. 9 (2019), https://doi.org/10.1063/1.5079394
[21] B.F. Yu, Q. Gao, B. Zhang, X.Z. Meng, Z. Chen, Review on research of room temperature magnetic refrigeration, Int. J. Refrig. 26 (2003) 622–636, https://doi.org/10.1016/S0140-7007(03)00048-3
[22] F. Körmann, D. Ma, D.D. Belyea, M.S. Lucas, C.W. Miller, B. Grabowski, M.H.F. Sluiter, "Treasure Maps" for magnetic high-entropy-alloys from theory and experiment, Appl. Phys. Lett. 107 (2015), https://doi.org/10.1063/1.4932571
[23] M. Kurniawan, A. Perrin, P. Xu, V. Keylin, M. McHenry, Curie temperature engineering in high entropy alloys for magnetocaloric applications, IEEE Magn. Lett. 7 (2016) 1–5, https://doi.org/10.1109/LMAG.2016.2592462
[24] Z. Rao, B. Dutta, F. Körmann, D. Ponge, L. Li, J. He, L. Stephenson, L. Schäfer, K. Skokov, O. Gutfleisch, D. Raabe, Z. Li, Unveiling the mechanism of abnormal magnetic behavior of FeNiCoMnCu high-entropy alloys through a joint experimental-theoretical study, Phys. Rev. Mater. 4 (2020), https://doi.org/10.1103/PhysRevMaterials.4.014402
[25] J.K.-P. E-Wen Huang, Guo-Yu Chang, Yeol Hung Soo, Lee, W.-C.Y. Jayant, P.K.L. Jing, J. Chou, Mechanical and magnetic properties of the high-entropy alloys for combinatorial approaches, 697–697, J. A. I. E. E 46 (2013), https://doi.org/10.1109/jaiee.1927.6535544
[26] N.A. Morley, B. Lim, J. Xi, A. Quintana-Nedelcos, Z. Leong, Magnetic properties of the complex concentrated alloy system CoFeNi0.5Cr0.5Alx, Sci. Rep. 10 (2020) 1–12, https://doi.org/10.1038/s41598-020-71463-3
[27] L. Han, Z. Rao, I.R. Souza Filho, F. Maccari, Y. Wei, G. Wu, A. Ahmadian, X. Zhou, O. Gutfleisch, D. Ponge, D. Raabe, Z. Li, Ultrastrong and ductile soft magnetic high-entropy alloys via coherent ordered nanoprecipitates, Adv. Mater. 33 (2021) 3–12, https://doi.org/10.1002/adma.202102139
[28] Z. Li, K.G. Pradeep, Y. Deng, D. Raabe, C.C. Tasan, Metastable high-entropy dual-phase alloys overcome the strength-ductility trade-off, Nature 534 (2016) 227–230, https://doi.org/10.1038/nature17981
[29] A. Perrin, M. Sorescu, M.T. Burton, D.E. Laughlin, M. McHenry, The role of compositional tuning of the distributed exchange on magnetocaloric properties of high-entropy alloys, JOM 69 (2017) 2125–2129, https://doi.org/10.1007/s11837-017-2523-3
[30] A. Quintana-Nedelcos, Z. Leong, N.A. Morley, Study of dual-phase functionalisation of NiCoFeCr-Alx multicomponent alloys for the enhancement of magnetic properties and magneto-caloric effect, Mater. Today Energy 20 (2021) 100621, https://doi.org/10.1016/j.mtener.2020.100621
[31] J. Rodriguez-Carvajal, Recent developments of the program FULLPROF, commission on powder diffraction, IUCr Newsl. 26 (2001) 12–19 ⟨http://www.iucr.org/iucr-top/comm/cpd/html/newsletter26.html⟩.
[32] P. Hohenberg, W. Kohn, Inhomogeneous Electron Gas, Phys. Rev. 136 (n.d.) B864–B871. https://link.aps.org/doi/⟨10.1103/PhysRev.136.B864⟩.
[33] W. Kohn, L.J. Sham, Self-consistent equations including exchange and correlation effects, A1133–A1138, Phys. Rev. 140 (1965), https://doi.org/10.1103/PhysRev.140.A1133
[34] A.V. Ruban, M. Dehghani, Atomic configuration and properties of austenitic steels at finite temperature: Effect of longitudinal spin fluctuations, Phys. Rev. B 94 (2016) 1–10, https://doi.org/10.1103/PhysRevB.94.104111
[35] O.K. Andersen O. Jepsen, G. Krier, Lectures on Methods of Electronic Structure Calculation, 1994.
[36] L. Vitos, H.L. Skriver, B. Johansson, J. Kollár, Application of the exact muffin-tin orbitals theory: the spherical cell approximation, Comput. Mater. Sci. 18 (2000) 24–38, https://doi.org/10.1016/S0927-0256(99)00098-1
[37] L. Vitos, Total-energy method based on the exact muffin-tin orbitals theory, Phys. Rev. B. 64 (2001) 14107, https://doi.org/10.1103/PhysRevB.64.014107
[38] L. Vitos, The EMTO Method and Applications in Computational Quantum Mechanics for Materials Engineers, Springer-Verlag, London, 2007.
[39] P.A. Korzhavyi, A.V. Ruban, I.A. Abrikosov, H.L. Skriver, Madelung energy for random metallic alloys in the coherent potential approximation, Phys. Rev. B 51 (1995) 5773–5780, https://doi.org/10.1103/PhysRevB.51.5773
[40] P. Soven, Coherent-potential model of substitutional disordered alloys, Phys. Rev. 156 (1967) 809–813, https://doi.org/10.1103/PhysRev.156.809
[41] B.L. Gyorffy, Coherent-potential approximation for a nonoverlapping-muffin-tin-potential model of random substitutional alloys, Phys. Rev. B 5 (1972) 2382–2384, https://doi.org/10.1103/PhysRevB.5.2382
[42] J.P. Perdew, Y. Wang, Accurate and simple analytic representation of the electron-gas correlation energy, Phys. Rev. B 45 (1992) 13244–13249, https://doi.org/10.1103/PhysRevB.45.13244
[43] D.M. Ceperley, B.J. Alder, Ground state of the electron gas by a stochastic method, Phys. Rev. Lett. 45 (1980) 566–569, https://doi.org/10.1103/PhysRevLett.45.566
[44] A.I. Liechtenstein, M.I. Katsnelson, V.A. Gubanov, Exchange interactions and spin-wave stiffness in ferromagnetic metals, L125–L128, J. Phys. F. Met. Phys. 14 (1984), https://doi.org/10.1088/0305-4608/14/7/007
[45] B. Skubic, J. Hellsvik, L. Nordstrom, O. Eriksson, A method for atomistic spin dynamics simulations: implementation and examples, J. Phys. Condens. Mattter. 20 (2008) 315203, https://doi.org/10.1088/0953-8984/20/31/315203
[46] O. Eriksson, A. Bergman, L. Bergqvist, J. Hellsvik, Atomistic Spin Dynamics, Oxford University Press, 2016, ⟨https://global.oup.com/academic/product/atomistic-spin-dynamics-9780198788669⟩.
[47] J.O. Andersson, T. Helander, L. Höglund, P. Shi, B. Sundman, Thermo-Calc & DICTRA, computational tools for materials science, Calphad Comput. Coupling Phase Diagr. Thermochem 26 (2002) 273–312, https://doi.org/10.1016/S0364-5916(02)00037-8
[48] C. Li, M. Zhao, J.C. Li, Q. Jiang, B2 structure of high-entropy alloys with addition of Al, J. Appl. Phys. 104 (2008), https://doi.org/10.1063/1.3032900
[49] J.D. Makinson, J.S. Lee, S.H. Magner, R.J. De Angelis, W.N. Weins, A.S. Hieronymus, X-ray diffraction signatures of defects in nanocrystalline materials, Adv. X-Ray Anal. 42 (2000) 407–411.
[50] S.F. Liu, Y. Wu, H.T. Wang, J.Y. He, J.B. Liu, C.X. Chen, X.J. Liu, H. Wang, Z.P. Lu, Stacking fault energy of face-centered-cubic high entropy alloys, Intermetallics 93 (2018) 269–273, https://doi.org/10.1016/j.intermet.2017.10.004
[51] A.J. Zaddach, C. Niu, C.C. Koch, D.L. Irving, Mechanical properties and stacking fault energies of NiFeCrCoMn high-entropy alloy, JOM 65 (2013) 1780–1789, https://doi.org/10.1007/s11837-013-0771-4
[52] M. Casas-Cabanas, M. Reynaud, J. Rikarte, P. Horbach, J. Rodríguez-Carvajal, FAULTS: a program for refinement of structures with extended defects, J. Appl. Crystallogr. 49 (2016) 2259–2269, https://doi.org/10.1107/S1600576716014473
[53] G. Laplanche, S. Berglund, C. Reinhart, A. Kostka, F. Fox, E.P. George, Phase stability and kinetics of σ-phase precipitation in CrMnFeCoNi high-entropy alloys, Acta Mater. 161 (2018) 338–351, https://doi.org/10.1016/j.actamat.2018.09.040
[54] Q. Yu, W.W. Xu, C. Cui, X. Gong, W. Li, L. Chen, X. Li, L. Vitos, Unveiling segregation-induced evolution in phase constitution of Cu-containing high-entropy alloys, J. Alloy. Compd. 843 (2020) 156109, https://doi.org/10.1016/j.jallcom.2020.156109
[55] A. Takeuchi, A. Inoue, Mixing enthalpy of liquid phase calculated by miedema's scheme and approximated with sub-regular solution model for assessing forming ability of amorphous and glassy alloys, Intermetallics 18 (2010) 1779–1789, https://doi.org/10.1016/j.intermet.2010.06.003
[56] A.K. Boer, F.R. de, Mattens, W.C.M. Boom, R. Miedema, A.R. Niessen, Cohesion in metals, Transit. Met. Alloy. (1988) 774.
[57] J.P. Perdew, K. Burke, M. Ernzerhof, Generalized gradient approximation made simple, Phys. Rev. Lett. 77 (1996) 3865–3868, https://doi.org/10.1103/PhysRevLett.77.3865
[58] Z. Dong, S. Huang, V. Ström, G. Chai, L.K. Varga, O. Eriksson, L. Vitos, MnxCr0.3Fe0.5Co0.2Ni0.5Al0.3 high entropy alloys for magnetocaloric refrigeration near room temperature, J. Mater. Sci. Technol. 79 (2021) 15–20, https://doi.org/10.1016/j.jmst.2020.10.071
[59] D.D. Belyea, M.S. Lucas, E. Michel, J. Horwath, C.W. Miller, Tunable magnetocaloric effect in transition metal alloys, Sci. Rep. 5 (2015) 1–8, https://doi.org/10.1038/srep15755
[60] K. Sarlar, A. Tekgul, I. Kucuk, Magnetocaloric properties of rare-earth-free Mn27Cr7Ni33Ge25Si8 high-entropy alloy, IEEE Magn. Lett. 10 (2019) 8–12, https://doi.org/10.1109/LMAG.2019.2955667
[61] J.Y. Law, L.M. Moreno-Ramírez, Á. Díaz-García, A. Martín-Cid, S. Kobayashi, S. Kawaguchi, T. Nakamura, V. Franco, MnFeNiGeSi high-entropy alloy with large magnetocaloric effect, J. Alloy. Compd. 855 (2021), https://doi.org/10.1016/j.jallcom.2020.157424